

NJC

Accepted Manuscript



This is an *Accepted Manuscript*, which has been through the Royal Society of Chemistry peer review process and has been accepted for publication.

Accepted Manuscripts are published online shortly after acceptance, before technical editing, formatting and proof reading. Using this free service, authors can make their results available to the community, in citable form, before we publish the edited article. We will replace this *Accepted Manuscript* with the edited and formatted *Advance Article* as soon as it is available.

You can find more information about *Accepted Manuscripts* in the [Information for Authors](#).

Please note that technical editing may introduce minor changes to the text and/or graphics, which may alter content. The journal's standard [Terms & Conditions](#) and the [Ethical guidelines](#) still apply. In no event shall the Royal Society of Chemistry be held responsible for any errors or omissions in this *Accepted Manuscript* or any consequences arising from the use of any information it contains.



Journal Name

ARTICLE

Solvent specific synthesis of nano corpse flowery Lithiated iron oxide as energy storage and gas sensing material

Rasmita Barik^a, K.T.Leung^b, Mamata Mohapatra^{a*}Received 00th January 20xx,
Accepted 00th January 20xx

DOI: 10.1039/x0xx00000x

www.rsc.org/

Iron oxide based material have been placed one of the most appealing matrices and promising futuristic materials for energy conversion/storage devices. Solvent dependent synthesis and growth of Lithiated iron oxide/LiFeO₂ nano flowers of was established by simple sol-gel method at low temperature. Herein for the first time the development of flowery (corpse flower) shape iron oxide based nano materials was reported. Effect of types of solvents on phase formation, shape and sizes of as synthesized samples are described using characterisation techniques such as X-ray diffraction, FTIR, Raman, Surface area, TEM, UV, and XPS. Li is incorporated into iron oxide matrix in ethylene glycol medium and developed as unique and uniform corpse flowery shape depending on various reaction parameters. Where as in presence of ethylene glycol mono methyl ether the shape of nano materials are completely changed. The supercapacitive and gas sensing properties of some selected synthesized materials are evaluated. Specific capacitance values of the materials were depended on the nature of the solvent and lithium content of the as prepared samples. The lithiated iron oxide samples exhibit a supercapacitance value of 241 F/g in 0.1M Na₂SO₄ between -0.4 and 1V versus Ag/AgCl. The gas sensing behaviour and optical properties are also included to open up the multidimensional applications of the samples.

1. Introduction

Iron oxides based materials are expected as excellent candidate for many futuristic advance applications due to their favourable physicochemical properties, chemical stability and non-toxicity.¹⁻⁶ Their inherent properties can be enhanced by careful controlled synthesis procedure with introduction of definite amount of various secondary metal ions. Insertion of alkali metal ion particularly lithium in iron oxides through the aqueous route is one of major interest for researchers now-a days. An iron oxide-based electrode, where only intercalation of Li ions occurs, has been recently found to be promising for cathode design.⁷ Li insertion resulted reduction of particle size and expansion of d-spacing between crystal layers of iron oxide.⁸ Therefore, lithiated iron oxide compounds particularly with rock-salt structure are of much interest for unique ionic conduction, electrical and electrochemical properties for use in

lithium-ion batteries to construct second-generation galvanic cells.⁹ Various synthetic methods were reported for preparation and structural modification of Li containing iron oxides.¹⁰ Among all solid-state reaction method or soft-chemistry method are preferred where H⁺/Li⁺ ion-exchange reaction occur in an alcoholic medium at a relatively low reacting temperature.¹¹ As these low temperature synthesis process are advantageous for getting smaller particle size of lithiated iron oxide which are found to be good candidate as electro active material.¹²⁻¹⁴ The various applications of iron oxides such as electrochemical properties and gas sensor can be enhanced by adopting solvent mediation precipitation routes due to their modified structure, morphology and phase.

The present work emphasizes development of synthetic protocols for lithium based iron oxide. A solvent mediated synthetic approach was chosen. Effect of both the nature of solvent and lithium ion on phase formation, crystal structure, electrochemical and gas sensing properties have been discussed.

2. Experimental

The chemicals used in the syntheses were Iron Nitrate Fe(NO₃)₃·9H₂O, Ethylene Glycol Mono Methyl Ether (CH₃O·CH₂·CH₂·OH) (EGME), Ethylene Glycol (EG) and Lithium hydroxide (LiOH) (E-Merck, India). All other chemicals were of AnLar grade. Samples

^a Hydro & Electrometallurgy Department, CSIR- Institute of Minerals and Materials Technology, BBSR- 751 013, Odisha, India, mamatamohapatra@yahoo.com

^b Prof. K. T. Leung, WATLab, Department of Chemistry, University of Waterloo, Waterloo, Ontario, Canada, N2L3G1

† Footnotes relating to the title and/or authors should appear here.

Electronic Supplementary Information (ESI) available: [details of any supplementary information available should be included here]. See DOI: 10.1039/x0xx00000x

were synthesized by adopting our previous synthesis method.¹⁵ Iron oxides materials were synthesized by following solvent mediated precipitation routes in presence of secondary metal ions namely Li. In this case desired solution of mixed metal ion (secondary metal ions + iron) was added to the calculated amount of solvent for fixed ratio. Desired amount of 0.1 M iron and Li ion solutions were vigorously stirred for 15 min in three necked flask attached with a condenser, thermometer and a pH meter (electrode). Stock solution of EGME or EG was added to the above solution (the ratio of solvent to total metal ion concentration was maintained 1:1) with continuous stirring to form a homogeneous solution for another 10 min. After that the solution was heated to desired temperature for 5 h, the flask was allowed to cool naturally to room temperature. The pH of the suspension was also monitored after the precipitation was completed. The yellow slurry after cooling was centrifuged and washed several times with deionized water and absolute alcohol and finally dried at 70°C for 24 hours in air oven. The iron analysis was done by using atomic absorption spectroscopy (AAS) of Perkin Elmer whereas Li analysis was done by ICP-OES (inductively coupled plasma-optical emission spectroscopy), Optima-2100DV, Perkin Elmer.

Crystal structures are determined by X-ray diffraction in PAnalytical model X'Pert PRO PW-3040/60 with Mo-K α radiation ($\lambda = 0.709$) at a scan speed of 1.2° min⁻¹ over a range of 5 to 40°. FTIR spectra were taken by Nicolet-670. Raman spectra were taken using a Renishaw (Renishaw plc, Gloucestershire, UK) in via Micro Raman Spectrophotometer equipped with 514 nm green laser having 1cm⁻¹ spectra resolution of Raman shift, X-Y step resolution of 0.1 μ m, and confocal resolution of 2.5 μ m. The laser output power on sample was set at 5.1 mW through the spectrum curve employing Lorentzian with FWHM. About 0.001gm of sample was taken for Raman analysis. The TEM micrographs were obtained using an electron microscope (FEI, TECNAI G2 20, TWIN) operating at 200 kV, equipped with a GATAN CCD camera. Samples for transmission electron microscopy (TEM) were prepared by first diluting a small amount of suspension with ethanol, sonicating and placing a single drop of the resulting suspension onto a 200 mesh carbon-coated copper grid, which was then allowed to dry in air. Selected area electron diffraction (SAED) patterns were obtained with the smallest area aperture available (10 μ m). The BET surface area and pore size were calculated by The solid samples were sonicated for 5 min with deionized water for complete dispersion and then analysis was done in UV-Visible spectrophotometer Perkin-Elmer. Cyclic voltgrams (CV) were performed in a three-electrode

cell workstation (CHI Instruments 660A). A standard Ag/AgCl electrode was used as the reference while a Platinum (pt) wire was used as the counter electrode. Cyclic-voltammograms were recorded using a computer-controlled CHI-660C electrochemical analyser (CHI, USA). Cyclic voltammetry studies were performed using a two compartment, three-electrode cell having a glassy carbon working electrode (area $\frac{1}{4}$ 0.07 cm²), a platinum electrode and Ag/AgCl (0.1 M Na₂SO₄) as the reference electrode in the potential range of 0 V to 0.85 V at a sweep rate of 5-100 mV/s. All the electrochemical experiments were carried out in an argon atmosphere. The synthesized materials were dispersed over a glassy carbon electrode with 0.1ml of 2% Nafion and dried prior to the electrochemical experiments.

The synthesized iron oxide was dispersed in isopropyl alcohol containing 50% of hydroxypropyl cellulose (HPC) of the material weight using an ultrasonic disperser for 20 min. This synthesized paste was deposited on the commercial Al₂O₃ substrate (15 mm 9 15 mm) with previously screen-printed gold electrodes (10 mm 9 10 mm) by a doctor blade technique and dried at 200°C for 1 h followed by baking in a furnace at 400°C for 1 h. The gas sensing activity of the device was investigated by using a home-made gas-sensing evaluation system equipped with digital mass flow controllers, a rapid heating system with programmed temperature controllers, and a quartz reactor for carrying out the sensing reactions. The change in resistance of the device due to the presence of target gas was measured using a high resistance meter (Keithley source meter 2400). The device was tested in the temperature range of 25–400°C at various concentrations of the target gas (100–500 ppm) in a temperature-controlled environment. The background gas was N₂, mixed with atmospheric air to have 10 % of oxygen content. The flow of gas (100 mL min⁻¹) over the sensor device was altered with the sample gas and dry air to record the sensor response in terms of electric resistance. The gas sensitivity is defined as the resistance ratio:

$$S = R_{air} - R_{gas}/R_{gas} \quad (1)$$

where R_{air} and R_{gas} are the electrical resistances for sensors in dry air and in gas, respectively.

3. Results and discussion

3.1 Chemical analysis

The different synthesized samples were named as Fe_{EGLi-1}, Fe_{EGLi-2}, Fe_{EGLi-3}, Fe_{EGLi-4} and Fe_{EGMELi-1}, Fe_{EGMELi-2}, Fe_{EGMELi-3}, Fe_{EGMELi-4} obtained through EG and EGME medium respectively. Samples

were synthesized by varying the concentration of lithium ion solution to iron solution at 1:9, 1:4, 1:2.33 and 1:1 ratio during precipitation of iron oxide using EG and EGME as solvent. The dark wine colour precursor solutions (mixture of iron and lithium) became visibly dark brown colour after precipitation. Figures S_{1a} and S_{1b} give the % of iron and lithium in lithiated iron oxide samples via EG and EGME synthesis media. The % iron and lithium precipitation from precursor are shown in Figures S_{1c} and S_{1d} respectively.

As shown in Figure 1a, % iron precipitated was more in presence of lithium for EG mediated precipitation routes as compare to EGME route. There was a slight variation in % iron precipitated with Li:Fe ratio. As observed from Figure 1b, lithium content in the precipitated products obtained in EG medium are slightly more as compared to that in EGME medium and in both the cases opposite trend is observed between lithium content in the solid product and Li ion used in the solution. Around 90% of iron is precipitated irrespective of lithium concentration and nature of solvent as shown in Figure S_{1c}. Whereas percentage of lithium precipitation was decreased with increase in Li content in the solution

3.2 XRD Study

The XRD patterns of different samples were given in Figure 1. The different planes observed for Fe_{EGLi-1} were assigned to (102), (104), (110), (113), (024), (116), (018), (214), (300), (1010) and (220) of α -Fe₂O₃ phase (ICDD: 01-084-0310). Besides the above mentioned peaks there were no other peaks found which could be assigned to the crystalline phases of lithium containing compounds.

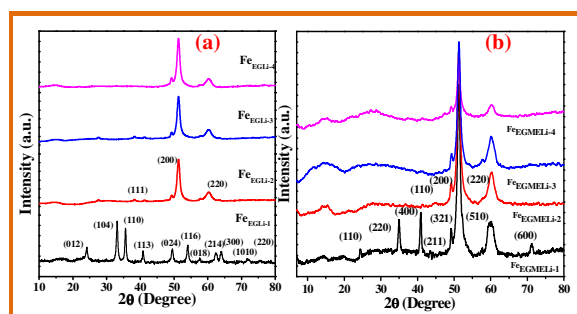


Figure 1. XRD patterns of as synthesised samples in presence of Li (a) EG and (b) EGME solvent mediated precipitation routes.

However, presence of lithium in chemical analysis indicated that in the sample Fe_{EGLi-1}, Li may be present either as amorphous or the phase which was XRD transparent. However, the XRD patterns of the samples Fe_{EGLi-2} to Fe_{EGLi-4} exhibited several peaks that could be

ascribed to α -LiFeO₂ phase and were indexed to the corresponding planes (110), (200) and (220) of this phase (JCPDS file No. 01-074-2284) confirming that these samples were purely crystalline α -LiFeO₂. The result is quite consistent with the results reported by several authors.¹⁶⁻¹⁷ The approximate crystallite sizes of the samples were calculated using the Debye–Scherer equation using the peak corresponding to (220) plane. The crystal sizes were found to be 10.04, 7.12 and 5.4 nm for the sample Fe_{EGLi-2}, Fe_{EGLi-3}, Fe_{EGLi-4}. Lithium ferrite is an inverse spinel compound where Li⁺ and Fe³⁺ ions occupy the octahedral B-sites. The synthesis is facilitated when the replacement of 2Fe²⁺ with Li⁺ Fe³⁺ in iron oxide complex is easier. In this case the reducing nature of solvent helps in the formation of LiFeO₂. Also the occupation of Li⁺ in interstitial positions would cause reduction of Fe³⁺. All the peaks showed shifts which increased with an increase in Li concentration due to topotactic incorporation of surface Li ions in the hematite matrix. It may also increase the crystallinity of the sample.^{10,18} Here, it has been noted that % metal ion precipitated along with iron is very less, therefore the Li:Fe ratio in the synthesised samples is lesser in stoichiometry ratio as compared to the theoretical Li:Fe ratio in LiFeO₂. Thus the signature peak for α -LiFeO₂ in XRD *i.e.* the peak corresponding to (220) and (111) planes shifted. However, there is hardly any effect on (200) plane. The observation is in contrast to previous reported results where it was mentioned that the doping in the above compound does not affect its (111) plane.¹⁹⁻²¹ The lattice parameter *a* was calculated as 4.149 Å which agreed with literature data for the pure phase formation.²⁰ Also the diffraction peaks were comparatively broader which indicated the smaller size of the crystallites.²¹ Figure 3 showed the change in relative intensities (RI) of (111) and (220) plane and their ratios in various samples obtained in EG medium. It was observed that RI as well as their ratios increased with increase in % of Li for EG mediated samples.

In case of EGME mediated samples, XRD patterns of Fe_{EGMELi-1} were well matched with LiFeO₂ in contrast to EG mediated sample with same Li:Fe ratio. Different planes (110), (220), (400), (211), (321), (510) and (600) were well matched with the JCPDS file No. 01-070-2711, whereas for Fe_{EGMELi-2} to Fe_{EGMELi-4} samples (110), (200) and (220) planes were well matched with JCPDS file No. 01-074-2284 as shown in Figure S₂. It is noted that, one broad peak was observed at around 2θ value of 14-15° which might be due to existence of reduced phases of iron oxides in these samples. Further characterisations were done to study the purity of synthesised phases. EGME creates the favourable environment for the possible formation of α -LiFeO₂. The crystal sizes were found to be 12.38,

11.54, 8.31 and 4.8 nm for the sample Fe_{EGLI-1}, Fe_{EGLI-2}, Fe_{EGLI-3} and Fe_{EGLI-4} respectively. A reverse trend in RI of (111) and (220) planes were observed for EGME mediated samples. The RI of (220) plane decreased with increase in % of Li. So the crystal growth was favourable in (200) direction. The crystallinity of the samples decreased as compare to EG mediated samples.

3.3 FTIR Study

The FTIR spectra of synthesized samples in both the media were shown in Figure 2. The presence of band at 1343 cm⁻¹ confirmed the presence of metal-solvent bonding in FeEGLI-1.¹³ It may be due to adsorption of complex solution over hematite surface. The band at 1642 cm⁻¹ was assigned to the bending mode of -OH (due to adsorbed water). Appearance of -OH bending mode at 894 cm⁻¹ was due to the transition moment lying in the *a-b* plane; another one at 791 cm⁻¹ corresponds to the transition moment parallel to *c* axis.^{9,21} For the present samples, both the peaks as mentioned above were shifted to 791 and 894 cm⁻¹. These two peaks gradually diminished and completely vanished in the samples prepared at higher Li:Fe ratios in both the media. An absorption bands at 543 cm⁻¹ present in FeEG series samples shifted to higher wavelength with increase in lithium content. This band falls in the range of primary band for pure Li ferrite in the range of 585–546 cm⁻¹.²² The positions of infrared bands are gradually shifted due to the shortening of bond length of the tetrahedral site by more intercalation of Li ion. Surprisingly this particular band is not seen in IR spectra of FeEGME series samples, rather than a band at 631 cm⁻¹ is visibly seen which is assigned to the longitudinal absorptions (Au) of hematite. The band at 631 cm⁻¹ is completely vanished at higher concentration of Li which is perhaps due to the synergistic effect of incorporation of lithium and variation in shape and sizes of the particles. The high frequency band at around 420 cm⁻¹ (encircled in Figure 4b) recorded only for FeEGME series samples. This band was

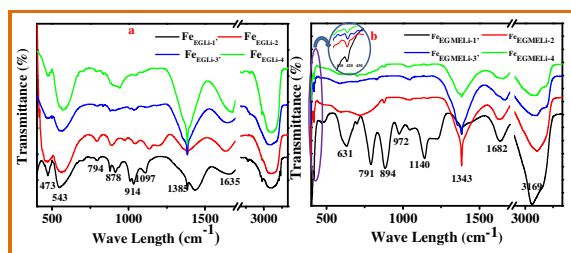


Figure 2. IR spectra of as synthesised samples in presence of Li (a) in EG and (b) EGME solvent mediated precipitation routes.

observed for Li₂CO₃ on the basis of ⁷Li - ⁶Li isotopic shifts²³ which was assigned to the LiO₄ tetrahedron (Li⁺ - O²⁻ complexes at the tetrahedral site). The intensity of this band goes on decreasing with increasing in the lithium content in the samples. The variation in the frequency range of IR bands was dependent on the microstructural properties of the sample.

3.4 Raman Study

To understand the phase formation of Fe₂O₃ and LiFeO₂ and arrangement of Li ion in those phases, Raman analysis was done. Raman spectra of all the synthesized samples are shown in Figure 3. Raman bands observed for the sample Fe_{EGLI-1} at 223 (A_{1g}), 292 (E_g), 408 (E_g), 498(A_{1g}) and 614(E_g) cm⁻¹ were assigned to hematite phase.²⁴⁻²⁵ These are attributed to the Fe-O stretching mode of FeO₆ octahedral linked to α-Fe₂O₃.²⁶ But these peaks were slightly shifted due to the presence of Li. The bands at 223 and 292 cm⁻¹ experienced greater broadening as compared to the remaining oxygen-related bands. So it could be clearly observed that the % Li doping plays significant role for the phase formation as discussed in XRD data. The peaks observed for other samples in EG medium at 253 and 581 cm⁻¹ are assigned to the Li-cage in an octahedral environment and these results are in good agreement with bulk α-LiFeO₂. Raman bands at 419 and 464 cm⁻¹ assigned to the LiO₄ tetrahedron.²⁶ The vibrational bands that appeared over 390-500 cm⁻¹ are assigned as internal modes of LiO₄.²⁶ Raman band at 720 cm⁻¹ was assigned to strong Fe-O stretching mode of lithium ferrite.⁴

The Raman spectra for EGME series samples were shown in Figure 3b. In case of Fe_{EGME1-1} five bands at 231, 304, 394, 474 and 687 cm⁻¹ were observed. These peaks could be attributed to the O-Fe-O bending and the Fe-O stretching

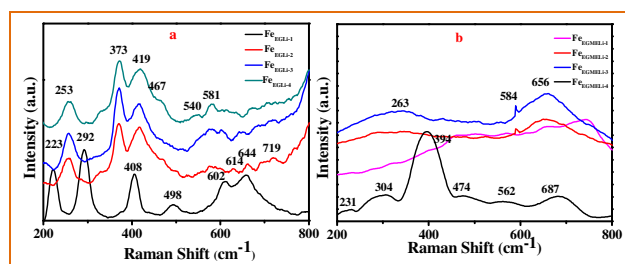


Figure 3: Raman bands (200-800 cm⁻¹) for synthesised LiFeO₂ in EG and (b) EGME solvent mediated precipitation routes.

mode of FeO₆ octahedra, respectively.²⁷⁻³⁰ Only three broad peaks were observed at 263, 584 and 656 cm⁻¹ corresponded to Li peaks for rest EGME series.³¹ The broadness in Raman band observed in (600-700 cm⁻¹) region might be due to the

overlapping of vibrations of the two types of cations at the same site.

3.5 Microstructure study: Insight mechanism

The TEM image and selected area electron diffraction (SAED) pattern of EG mediated Li doped iron oxide samples $\text{Fe}_{\text{EGLi-1}}$ and $\text{Fe}_{\text{EGLi-4}}$ were shown in Figure 4 and Figure 5 respectively.

Hematite phase with 20-30 nm nano rods and nano flower were clearly observed from. The selected area electron diffraction (SAED) pattern in Figure 4c and Figure 4c suggested that the sheet is a single-crystal, and the crystal structure can be indexed to a hexagonal type of $\alpha\text{-Fe}_2\text{O}_3$. Close-packed Fe_2O_3 flowers were also observed. The porous structure was observed either between the granules or the flowers petals. The sheets are randomly assembled and were irregular-shaped, but they grow from the same root and appear as Plumeria or Frangipani. The petal has a shape of trapezoid and having smooth surface. But with the increase in % Li the complete formation of nano flowers appeared as shown in Figure 4b and Figure 5b. They were looking alike as Corpse flower which is scientifically named as “*Rafflesia arnoldii*” shown as inset Figure. The petals have an average length of about 50 nm. Interestingly, the self-assembly ordered array of LiFeO_2 was observed due to its functionalized surface by EG. Self-assembly of EG-iron oxide crystals occurred via slow evaporation of solvent in the solution of iron oxide particles. This phenomenon

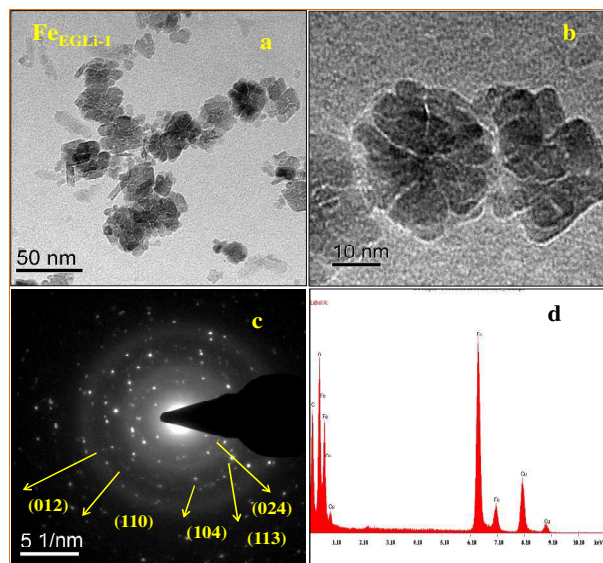


Figure 4. (a) and (b) TEM images, (c) SAED pattern and (d) EDAX $\text{Fe}_{\text{EGLi-1}}$ samples.

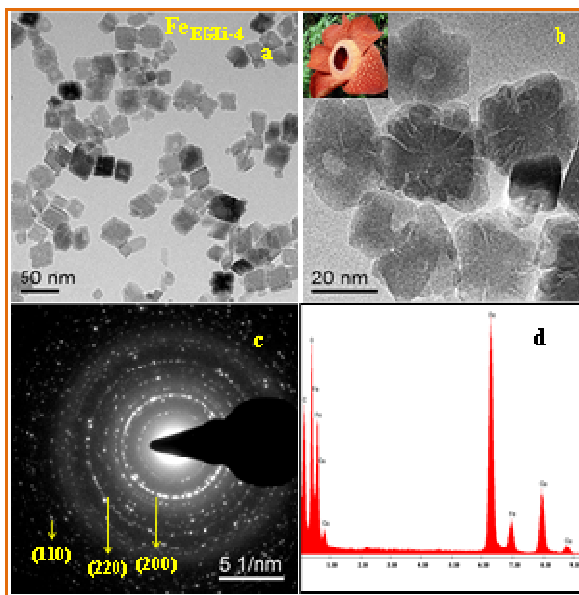


Figure 5. (a) and (b) TEM images, (c) SAED pattern and (d) EDAX $\text{Fe}_{\text{EGLi-4}}$ samples.

arise from van der Waals interaction among OH group of EG at the surface. Hole in central part of flower is formed due to overall etching reaction. Cationic exchange reaction occurs during transformation of hematite to LiFeO_2 and the dissolution of Fe_2O_3 in alkali condition occurred due to low release of ionic precursors such as Fe^{2+} and Li^+ ions which are the driving force for the reductive etching reaction of Fe^{3+} ion due to the higher Lewis acidity. In the presence of Li^+ ion on the surface of hematite, reduction of iron (II) and inclusion of Li occur at the same time through transportation of oxygen from iron (II) to Li ion. During the reaction time, hollow structure was formed with crystalline state of iron oxide. The SAED pattern shown in Figure 6c where all of the ring spots were evaluated to represent d-spacing's of 0.24, 0.20, and 0.14 nm, which could be referred to the crystallographic directions of (111), (200) and (220) respectively. These results were also consistent with the standard information provided by the XRD patterns. Corresponding EDAX is shown in Figure 4d and Figure 5d. It shows the ratio of O to Fe in the sample matched to the theoretical ratio of O to Fe in LiFeO_2 material. Only Fe and O are shown and due to the low atomic number Li couldn't be detected by EDAX.

In case of EGME mediated Li containing iron oxide samples tiny nanoparticles up to 5nm was observed for $\text{Fe}_{\text{EGMELi-1}}$ as shown in Figure 6a. Also it is clearly observed that the resulting product has average diameter of 2.5 nm and

average length of 5 nm and a fairly narrow particle size distribution range which supports the XRD results. The nanoparticles could have spheroidal shape. The SAED pattern shown in Figure 6c well matched with the crystal planes as shown in corresponding XRD patterns. Whereas with the increase in % Li the sample showed the decreased particle size with narrow size distribution as shown in Figure 7. The particles showed development of small random tiny particles over bigger particle as base. The nanoparticles could have

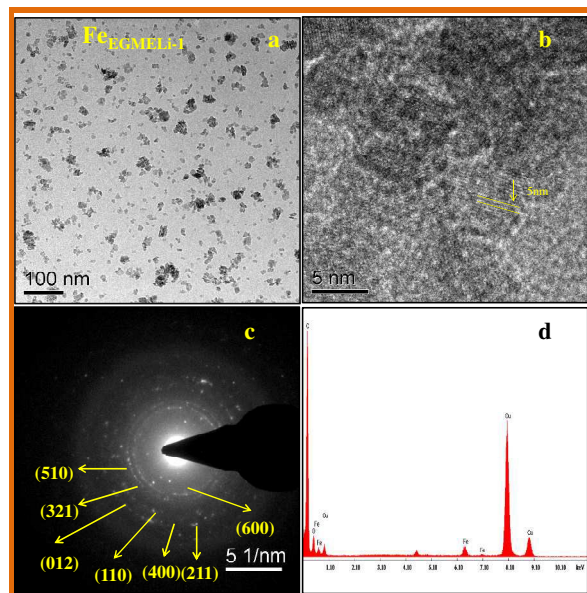


Figure 6. (a) TEM, (b) HRTEM (c) SAED pattern and (d) EDAX of $\text{Fe}_{\text{EGMELI-1}}$ sample.

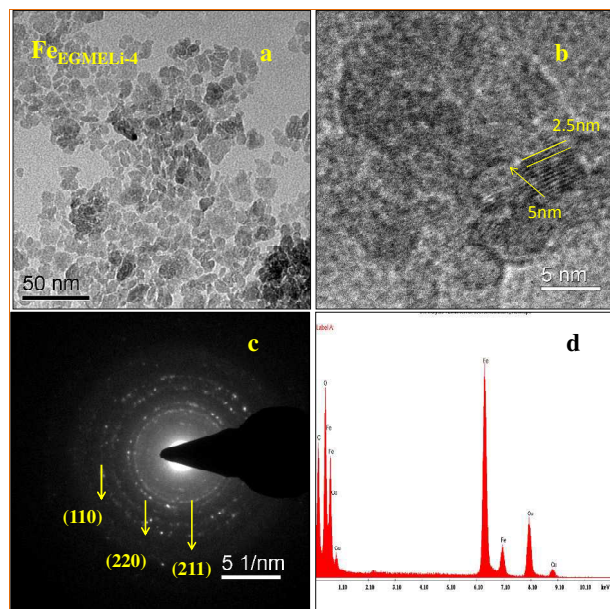


Figure 7. (a) TEM, (b) HRTEM, (c) SAED pattern and (d) EDAX of $\text{Fe}_{\text{EGMELI-4}}$ sample.

spheroidal shape. The formation of nanoparticles can be generally attributed interfacial energy and the magnetic dipole-dipole interaction.³² To get an insight into the growth and self-assembly of nano particles, HRTEM the fringes are shown in Figure 7b which shows an average size of d spacing are 5 nm and 2.5 nm and well matched with the crystal planes of the corresponding phase confirmed in XRD study. Also the EDAX study in Figure 6d and 7d indicated the observed atomic ratio of Fe and oxygen match to that of theoretical value for LiFeO_2 compound confirming the pure phase formation.

3.6 Surface area study

The surface area and pore size distribution of $\alpha\text{-Fe}_2\text{O}_3$ -based nanostructures and the LiFeO_2 materials were calculated through N_2 adsorption-desorption measurement. The Brunauer-Emmett-Teller (BET) surface areas of the samples in both the solvent media were estimated and are given in Table S₁. In the case of sample $\text{Fe}_{\text{EGLI-1}}$, as shown in Figure 8, characteristic type IV isotherm was observed with type H3 distinct and broad hysteresis loop at a relative pressure P/P_0 of 0.9 to 1. The surface area value of $123.9 \text{ m}^2/\text{g}$ was estimated. Corresponding hysteresis loop may be associated

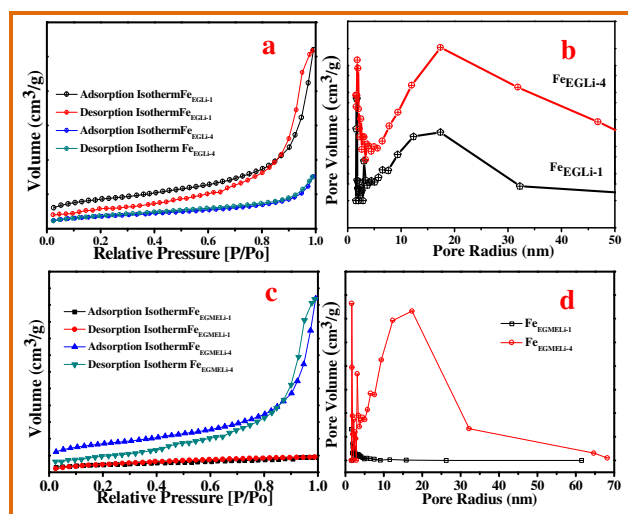


Figure 8. (a) Surface area and (b) pore size distribution plots of $\text{Fe}_{\text{EGLI-1}}$ and $\text{Fe}_{\text{EGLI-4}}$ (c) Surface area and (d) Pore size distribution plots of $\text{Fe}_{\text{EGMELI-1}}$ and $\text{Fe}_{\text{EGMELI-4}}$.

with aggregates of thorny particles forming slit-like pores. Based on the BJH calculation, the pore size distributions (Figure 8b) of $\text{Fe}_{\text{EGLI-1}}$ was 12.13 nm, indicating homogeneity of the pores. These pores arise from the void space generated during the oriented organization of nanocrystals.

In contrast, the more flowery structure-like nano architecture of $\text{Fe}_{\text{EGFeLi-4}}$ showed a relatively low surface area of $40.86 \text{ m}^2/\text{g}$ and small absorbance of N_2 in Figure 8c, with a typical H3-type hysteresis loop at a relative pressure P/P_0 of 0.9 to 1.0. The shifting of relative pressure towards high value suggests that the pore distribution might originate from the holes between compactly packed primary nanocrystals and the large mesoporous distribution, or it might originate from some vacancies caused by the absence of subunits.³¹ However, almost the same pore-size distribution of around 10 nm was observed from the BJH analysis (Figure 8d), indicating that small pores exist in both the nanostructures. The characteristic N_2 adsorption-desorption isotherms and pore size distributions revealed that both samples have mesoporous structures. $\text{Fe}_{\text{EGMELi-1}}$ has shown the surface area $105.1 \text{ m}^2/\text{g}$ and has broad H3-type hysteresis loop as compared to that of $\text{Fe}_{\text{EGMELi-4}}$ (surface area value- $38.33 \text{ m}^2/\text{g}$) at a relative pressure P/P_0 of 0.85–1.0. The BJH analyses showed that the sample possessed bimodal (small and large) mesoporous distribution, having a mean pore size of 5–8 nm.

3.7 XPS study

X-ray photoelectron spectroscopy (XPS) was used to further confirm surface phenomena of the synthesized samples. XPS spectra of $\text{Fe}_{\text{EGLi-4}}$ are shown in Figure 9. The XPS spectrum for iron is split by the $\text{Fe}2p$ spin-orbit effect into the $2p_{3/2}$ and $2p_{1/2}$ components. The $2p_{3/2}$ and $2p_{1/2}$ signals were accompanied by typical satellite peaks at 719 eV. The binding energy for $\text{Fe} 2p_{3/2}$ was estimated as 711.3 eV, the value is comparable with binding energy (BE) value of the $2p_{3/2}$ peak in Fe_2O_3 for Fe(III) ^{32–35}, confirms the presence of iron as hematite phase in the sample. Furthermore, BE difference between O_{1s} was also agreed with the expected value. The obtained O/Fe atomic ratio is 1:4. The asymmetry of the O_{1s} peak on its higher BE side (Figure 9b suggest the presence of surface hydroxyl groups. In principle, these OH groups can be classified according to three different types: free or isolated OH groups, H-bonded OH groups and OH groups interacting with chemisorbed water molecules. It could be assigned to different chemical states such as hydroxyl, two peaks were also observed in the O_{1s} region. The broad and lower intensity peak near 531.0 eV is complex and could be assigned to different chemical states such as hydroxyl, water species or precursor impurities for LiFeO_2 .³⁶ Li_{1s} signal was observed at 56eV which is typical value for Li^+ species. So the LiFeO_2 oxide formation was confirmed.^{37–39}

Similar observations were obtained for the EGME mediated samples. There was no significant change as compare to EG mediated samples. Figure 11d shows the binding energies of $\text{Fe} 2p_{3/2}$ and $\text{Fe} 2p_{1/2}$ as 711.3 and 725.3 eV, respectively. Due to the presence of Li the slight shift in binding energy was observed. Two O_{1s} peaks were obtained in higher BE side due to the presence of surface hydroxyl groups in $\text{Fe}_{\text{EGMELi-4}}$ sample. Li_{1s} signal was observed at 56eV.

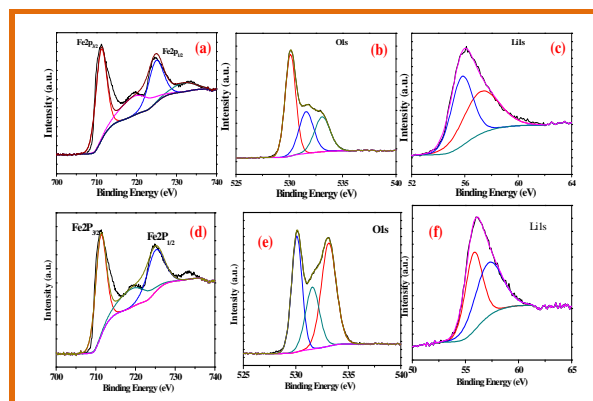


Figure 9. XPS spectra of $\text{Fe}_{\text{EGLi-4}}$, (a) $\text{Fe} 2p$, (b) O_{1s} and (c) Li_{1s} and XPS spectra of $\text{Fe}_{\text{EGMELi-4}}$, (d) $\text{Fe} 2p$, (e) O_{1s} and (f) Li_{1s} .

3.8 Optical properties

The optical absorption properties of the as synthesized samples were investigated at room temperature by the UV-Vis spectra and have been represented in Figure 10. The UV-Vis spectra was taken the range of 200–700nm. The two types of optical absorptions in the UV and visible regions are mainly attributed the direct charge transition of $\text{O}_2^- 2p \rightarrow \text{Fe}^{3+} 3d$ (UV absorption), and the latter originates from the indirect charge transition of $\text{Fe}^{3+} 3d \rightarrow 3d$ (visible absorption).^{40,41}

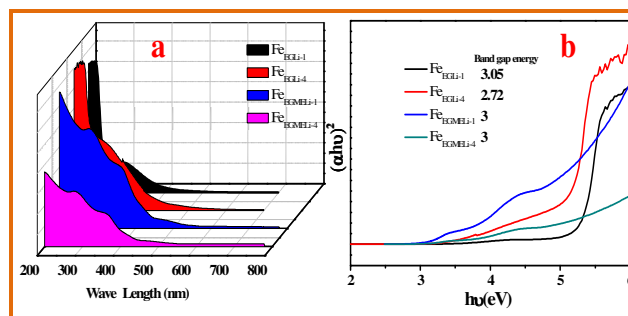


Figure 10. (a) UV-visible absorption spectra of synthesized samples, (b) plot of $(\alpha h\nu)^2$ versus photon energy for direct transition.

For sample $\text{Fe}_{\text{EGLi-1}}$, it revealed that two absorption edges observed around with sharp edge at 256 nm and 394nm. The

band gap energy 3.05 eV was estimated for the Fe_{EGLi-1} sample whereas the band gap energy of Fe_{EGLi-4} slightly decreased as compare to Fe_{EGLi-1} due to the higher percentage doping of Lithium. However the band gaps are found to be same for the samples obtained in EGME medium.

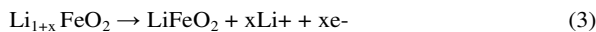
3.9 Electrochemical Properties

To evaluate the rate capability, the tests at different discharge current were conducted for Li doped synthesized nanomaterial. The electrochemical performances of the samples were evaluated by following the procedure as described in experimental section. The cyclic voltametric tests for the samples prepared in presence of Li in EG and EGME medium were carried out with neutral electrolytes 0.1 M Na₂SO₄ in the range of -0.4 to 1 Volt and results are shown in Figure 11 and 12 respectively. The specific capacitance values were calculated using the following Equation [2].

$$C_s = I\Delta t/m\Delta V \quad (2)$$

Where I is the discharge current, Δt is the discharging time period in seconds m is the mass of the electro active materials and ΔV is the potential difference. The 1D nano materials normally showed excellent supercapacitance behaviour. The possible electron transfer may occur through 1D material. However, in presence of lithium, both phase and shape of the samples obtained in the studied solvent mediated precipitation routes are completely different. Here in EG medium, as synthesised LiFeO₂ phase is of flowery shape without and with a prominent whole in the centre of flower developed in low and high lithium concentration respectively. This unusual shape of the materials along with high surface area value may affect the electrochemical properties of the materials. Again, the alkali metal ion plays a vital role in specific capacitance value. The redox coupling of iron oxide was developed with lower % of Li in the matrix, whereas higher % of Li, lowered value of specific capacitance value was observed. Two redox peaks were observed due to the reducing nature of EG environment. Fe⁺² to Fe⁺³ electron transfers occurred in presence of Li⁺. The peak at -0.089V corresponded to the Li redox coupling whereas at 0.4 V peak corresponded to the Fe peak. The pseudo capacitance behavior is due to the combined effect of the redox reaction. The pseudo capacitive behavior could also be due to the diffusion of electrolyte ions in different channels present in the porous nanostructures.³⁹ As given in Figure 11 the pseudo capacitor nature of curve was change to electric double layer

with increase in doping percentage. FeEGLi-1 sample shows specific capacitance of 241 F/g. The peak observed at 0.5 V in CV curves indicates Li ion intercalation in to the iron matrix.⁴⁰ Possible electrochemical reaction occurred in the α -LiFeO₂ cathode due to charge–discharge of Fe³⁺/Fe²⁺.⁴⁰⁻⁴²



It is likely that due to this reason the α -LiFeO₂ sample shows

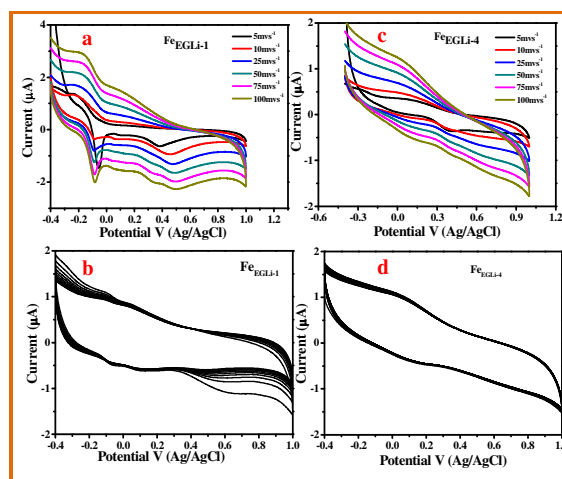


Figure 11. (a) CV curve of FeEGLi-1 using 0.1M Na₂SO₄ as electrolyte, (b) CV of FeEGLi-1 for 500 cycles at 100 mVs⁻¹, (c) Cyclic voltammetry curve of FeEGLi-4 using 0.1M Na₂SO₄ as electrolyte and (d) CV of FeEGLi-4 for 500 cycles at 100 mVs⁻¹.

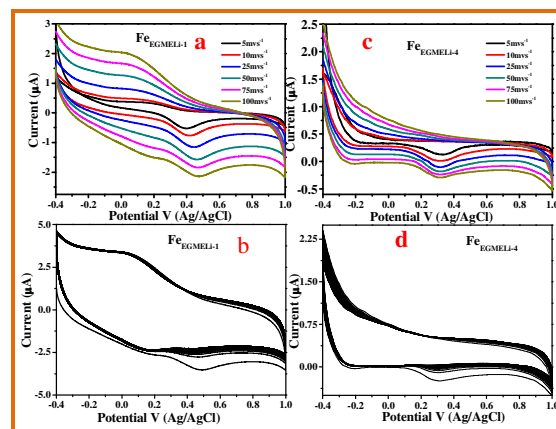


Figure 12. (a) CV curve of FeEGMELi-1 using 0.1M Na₂SO₄ as electrolyte, (b) CV of FeEGMELi-1 for 500 cycles at 100 mVs⁻¹ (c) CV curve of FeEGMELi-4 using 0.1M Na₂SO₄ as electrolyte, (d) CV of FeEGMELi-4 for 500 cycles at 100 mVs⁻¹.

higher specific capacitance value. However, sample having more Li incorporation is showing less specific capacitance value. One significance change in CV curve was observed with the increase in % Li that the pseudo-capacitance nature CV curve is changed to Electrical double layer nature CV curve.

The capacitance behaviors of different materials are conditional to their cation characteristics and crystalline states⁴³⁻⁴⁵ *i.e.*, the ionic electronegativity of constituent cations and closely related to the BET the surface area value. The specific capacitance values are mentioned in Figure S₃.

The cycling stability of Fe_{EGLi-1}, Fe_{EGLi-4}, Fe_{EGMELi-1} and Fe_{EGMELi-4} electrodes were examined for 200 cycles at a specific current density of 5 mA g⁻¹ as shown in Figure 11(b&d) and Figure 12 (b&d). The Fe_{EGLi-4} sample showed better super capacitance behavior with the retention percentage was 98% up to 200 cycles. The specific capacitance slightly decreased for the Fe_{EGLi-4} sample, whereas for the Fe_{EGLi-1} sample the value remained almost constant. The similar observations were made for the EGME sample (Figure 12). In EGME series, Fe_{EGMELi-1} sample showed better super capacitance behavior with retention percentage was 98% up to 200 cycles. From the above said observation, it can of the samples are affected by % lithium in synthesized LiFeO₂ irrespective of solvent media. The charge–discharge plots for Fe_{EGLi-1}, Fe_{EGLi-4}, Fe_{EGMELi-1} and Fe_{EGMELi-4} samples at current density 5 mA g⁻¹ was shown in Figure 13. The discharge capacity remains constant for all the samples.

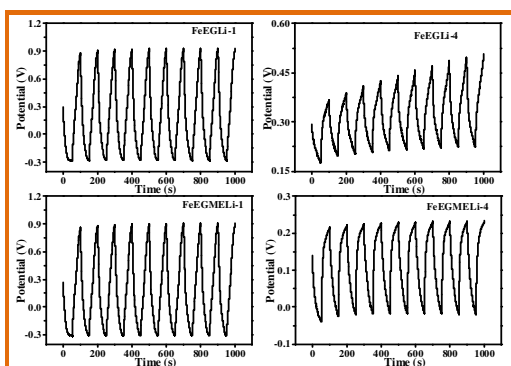


Figure 13. Typical charge–discharge plots for Fe_{EGLi-1}, Fe_{EGLi-4}, Fe_{EGMELi-1} and Fe_{EGMELi-4} samples at current density 5 mA g⁻¹. The nature of the curve shows linear variation of the voltage during the charging–discharging process.

3.10 Gas sensor study

Gas sensor property in LiFeO₂ may be developed due to electron jumping between the two valence state of iron, Fe²⁺ and Fe³⁺ on the octahedral sites in the spinel lattice structure.³⁷ Considering the high surface area and inherent porosity gas sensing ability of Fe_{EGLi-1} and Fe_{EGMELi-1} samples for different toxic gases (HCHO, C₂H₅OH and CO) were studied at a concentration of 500 ppm at 250, 300, and 350°C shown in Figure 14 and 15 respectively. It was observed that the selected

samples exhibited highest responses to ethanol and good response towards formaldehyde and weak response for carbon monoxide. At 350°C, HCHO and CO showed sensitivity of 0.73 and 0.16 for 500 ppm, respectively,

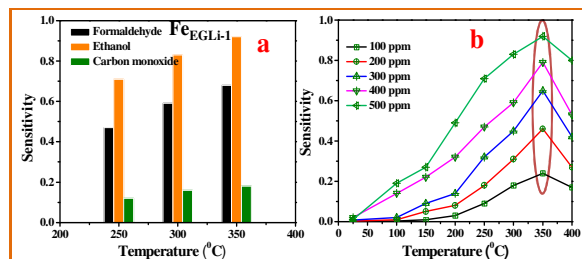


Figure 14. Sensitivity of the sensors based on the Fe_{EGLi-1} sample (a) comparative sensor performance for HCHO, C₂H₅OH and CO (b) as a function of the C₂H₅OH concentration at different temperature.

Whereas for C₂H₅OH, the sensitivity was 0.92 for Fe_{EGLi-1} sample. Gas sensitivity was calculated by the formula Equation [1]. The response curve shown in Figure 15 showed a parabolic-shape in the entire test range with highest sensitivity (for 500 ppm) observed at 350°C in the linear range. Excellent sensing properties for ethanol shown could be due to its porous structure associated with the small grain size, which enable C₂H₅OH gas to access more surfaces of the porous flowery material contained in the sensing unit. Therefore, the higher surface area for the nanostructure sample provides more chances to adsorb and desorb C₂H₅OH gas molecules which lead higher sensitivity at high temperature.^{25,39} However, Fe_{EGLi-4} sample showed very negligible sensitivity towards toxic gases might be due to having less surface area.

Similarly for Fe_{EGMELi-1} sample gas sensing behavior is shown in Figure 15. C₂H₅OH and CO showed sensitivity of 0.56 and 0.18 for 500 ppm at 350°C respectively, whereas for HCHO, the sensitivity was found to be 0.87. Fe_{EGMELi-1} exhibited a maximum response to ethanol at 350°C. According to gas sensor principle diffusion of gases into the porous sample were independent on the working temperature, but dependant on the porosity within the sample. Similar to Fe_{EGLi-4}, Fe_{EGMELi-4} didn't show better sensitivity towards any toxic gases. The present method offers a simple solvent mediated synthesis routes for preparation of LiFeO₂ phase which can be utilized for multi-application as shown in Figure 16. A comparison study on the synthesis routes and the application of LiFeO₂ (Table S₂) was made with reported literature synthesis method to evaluate the novelty of our method.

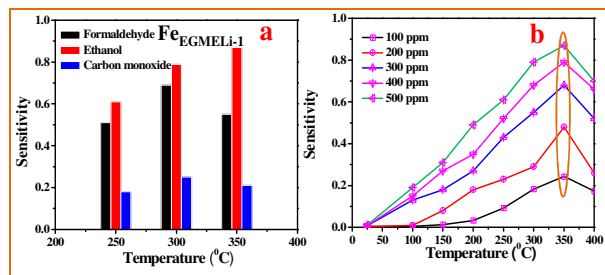


Figure 15. Sensitivity of the sensors based on the Fe_{EGMELi-1} (a) comparative sensor performance for HCHO, C₂H₅OH and CO, (b) Effect of C₂H₅OH concentration at different temperature.

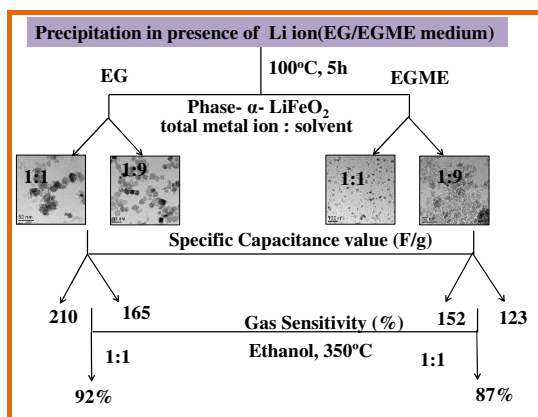


Figure 16. Schematic presentation of results obtained from the EG and EGME synthesis mediated synthesis of iron oxide in presence of Li.

4. Conclusions

In conclusion, α -LiFeO₂ has been synthesized for the first time in EG and EGME solvent medium at ambient temperature by varying the amount of amount of LiOH, H₂O and iron nitrate solutions series of samples are prepared by varying with Li/Fe molar ratio from 1:9 to 1:1. Around 90% of iron precipitated irrespective of lithium concentration and solvent whereas percentage of lithium precipitation decreased with increase in Li content in the solution. α -LiFeO₂ phases were developed irrespective of Li: Fe ratio. The relative intensities (RI) of (111) and (220) plane increased with the increased in % of Li for EG mediated samples and reverse effect is observed for EGME mediated samples. In EG medium, depending on the concentration of Li nano flowers with and without hole at central part of flower were formed. While in case of EGME, tiny nanoparticles up to 5nm for Fe_{EGMELi-1} were observed with narrow size distribution. The charge–discharge behavior investigation of the prepared α -LiFeO₂ nano particles as cathode materials

showed that the sample obtained in EG medium has more specific capacitance value than the sample obtained EGME medium. The nature of CV curve changed from pseudo capacitive to electrical double layer as lithium content increase in Li:Fe precursor solution. The FeEGLi-1sample showed sensitivity of 0.73 at 500 ppm, for HCHO whereas for C₂H₅OH, the sensitivity was 0.92. Similarly for FeEGMELi-1 sample, gas sensitivity of 0.56 and 0.18 are obtained for C₂H₅OH and CO (500 ppm) respectively, whereas for HCHO, the sensitivity was found to be 0.87. In both the solvent media, lithium containing samples showed better sensor for ethanol. Therefore the present study provides potentialities of some of the synthesised samples as electrode and sensing materials for high performance devices.

Acknowledgements

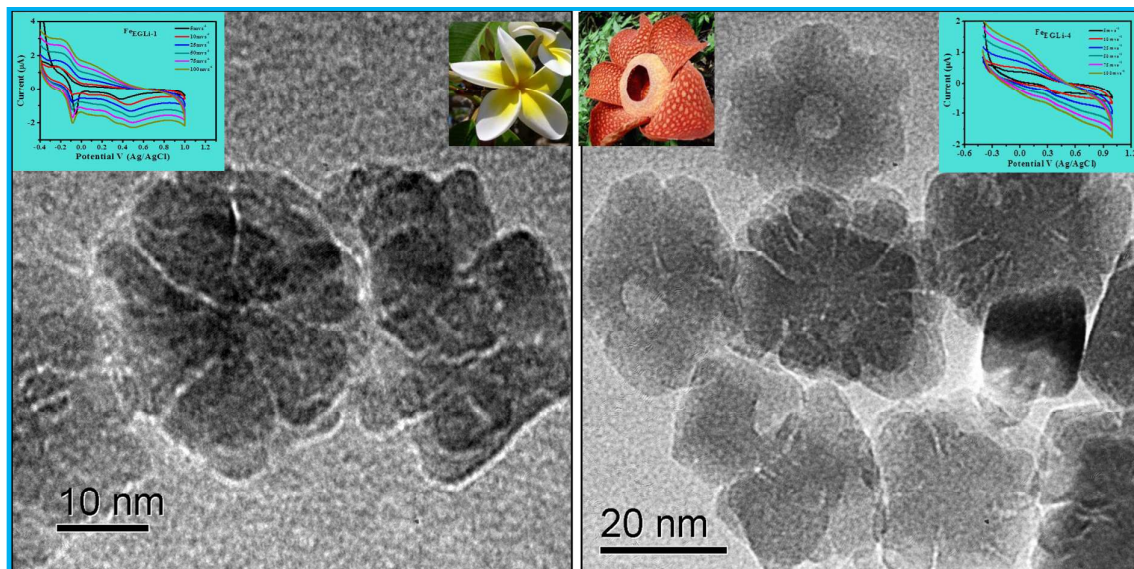
The authors are thankful to the Prof. B.K. Mishra, Director, Institute of Minerals and Materials Technology, Bhubaneswar, for his kind permission to do the research work. The authors wish to thank Dr. I. N. Bhattacharya, Head Hydrometallurgy Department. One of the authors (Rasmita Barik) is thankful to DST Inspire Division (Govt. of India) for their financial support.

References

- 1 K. Li, H. Chen, F. Shua, K. Chen and D. Xue, *Electrochimica Acta*, **2014**, 136, 10–18.
- 2 K. Chen, S. Yin and D. Xue, *Nanoscale*, **2015**, 7, 1161-1166.
- 3 X. Chen, K. Chen, H. Wang and D. Xue, *Electrochimica Acta*, **2014**, 147, 216–224.
- 4 X. Chen, K. Chen, H. Wang, S. Song and D. Xue, *Cryst Eng Comm*, **2014**, 16, 6707–6715.
- 5 K. Y. Li, J. J. Shao and D. F. Xue, *Mater. Res. Innovations*, **2013**, 17, 218-223.
- 6 K. Li, H. Chen, F. Shua, D. Xue and X. Guo, *RSC Adv.*, **2014**, 4, 36507–36512
- 7 B. Koo, H. Xiong, M. D. Slater, V. B. Prakapenka, M. Balasubramanian, P. Podsiadlo, C. S. Johnson, T. Rajh and E. V. Shevchenko, *Nano Lett.*, **2012**, 12, 2429–2435.
- 8 D. W. Junga, S. W. Hana, B. S. Kong and E. S. Oha, *J. Power Sources*, **2013**, 242, 357–364.
- 9 Y. Han, Y. J. Wang, L. Li, Y. P. Wang, L. F. Jiao, H. T. Yuan and S. X. Liu, *Electrochim. Acta.*, **2011**, 56, 3175–3181.

- 10 A. E. Abdel-Ghany, A. Mauger, H. Zaghib, and C. M. Julien, *J. Power Sources*, **2012**, 197, 285-291.
- 11 Y. Sakurai, H. Arai, S. Okada and J. I. Yamaki, *J. Power Sources*, **1997**, 68, 711-715.
- 12 L. Croguennec, P. Deniard and R. Brec, *J. Electrochem. Soc.*, **1997**, 144, 3323-3330.
- 13 S. Zeng, K. Tang, T. Li, Z. Liang, D. Wang, Y. Wang, Y. Qi and W. Zhou, *J. Phys. Chem. C.*, **2008**, 112, 4836-4843.
- 14 J. Wang, Y. Zhou, Y. Hu, R. O'Hayre and Z. Shao, *J. Mater. Sci.*, **2013**, 48, 2733-2742.
- 15 R. Barik, B. Pandey, S. Anand and M. Mohapatra, *J. Mater. Chem. A*, **2014**, 2, 12380-12389.
- 16 Y. Ma, Y. Zhu, Y. Yu, T. Mei, Z. Xing, X. Zhang and Y. Qian, *Int. J. Electrochem. Sci.*, **2012**, 7, 4657-4662.
- 17 X. Wang, L. Gao, F. Zhou, Z. Zhang, M. Ji, C. Tang, T. Shen and H. Zheng, *J. Cryst. Growth*, **2004**, 265, 220-223.
- 18 R. Collongues and G. Chaudron, *Compt. Rend. Acad. Sci. (Paris)*, **1950**, 124, 143.
- 19 Y. Wang, J. Wang, H. Liao, X. Qian, M. Wang, G. Song and S. Cheng, *RSC Adv.*, **2014**, 4, 3753-3757.
- 20 A. M. Rahman, A. M. Glushenkov, Z. Chen, X. J. Dai, T. Ramireddy and Y. Chen, *Phys. Chem. Chem. Phys.*, **2013**, 15, 20371-20378.
- 21 Y. Wang, J. Wang, H. Liao, X. Qian, Y. Zhu and S. Cheng, *Int. J. Electrochem. Sci.*, **2013**, 8, 8730-8739.
- 22 S. A. Mazen, M. H. Abdallah, R. I. Nakhla, F. Metawe, and H. M. Zaki, *Mater. Chem. Phys.*, **1993**, 34, 35-40.
- 23 K. S. Lee, J. H. Ko and V. H. Schmidt, *J. Korean Phy. Society*, **2005**, 46, 198-205.
- 24 I. V. Chernyshova and A. S. Madden, *Chem. Chem. Phys.*, **2007**, 9, 1736-1750.
- 25 P. Makie, G. Westin, P. Persson and L. Osterlund, *J. Phys. Chem. A*, **2011**, 115, 8948-8959.
- 26 S. H. Shim and T. S. Duffy, *Am. Mineral*, **2002**, 87, 318-326.
- 27 A. M. Jub and H. C. Allen, *ACS Appl. Mater. Interface*, **2010**, 2, 2804-2812.
- 28 J. A. Glasscock, P. R. F. Barnes, I. C. Plumb, A. Bendavid and P. J. Martin, *Thin Solid Films*, **2008**, 516, 1716-1724.
- 29 R. Barik, S. K. Tripathy and M. Mohapatra, *J. Mater. Sci.*, **2014**, 49, 5345-5354.
- 30 D. Bersani, P. P. Lottici, Montenero, *J. Raman Spect.*, **1999**, 30, 355-360.
- 31 V. I. Tyutyunnik, *J. Raman Spectrosc.*, **2000**, 31, 559-563.
- 32 X. Fei, Z. Z. Sao and X. Chen, *J. Mater. Chem. B*, **2013**, 1, 213-220.
- 33 C. Z. Wu, Y. Xie, L. Y. Lei, S. Q. Hu, C. O. Yang, *Adv. Mater.*, **2006**, 18, 1727-1732.
- 34 G. Carraro, D. Barreca, E. Comini, A. Gasparotto, C. Maccato, C. Sadad and G. Sberveglieri, *Cryst. Eng. Comm.*, **2014**, 14, 6469-6476.
- 35 T. Fujii, F. M. F. de Groot and G. A. Sawatzky, *Phys. Rev B*, **1999**, 59, 4, 3195.
- 36 L. Ferretto and A. Glisenti, *J. Mol. Cat. A*, **2002**, 187, 119-128.
- 37 Martı́n, E. Navarrete, J. Morales, C. Roldan, J. R. Ramos-Barradob and Luis Sanchez, *J. Mater. Chem.*, **2010**, 20, 2847-2852.
- 38 I. V. Chernyshova, S. Ponnurangam and P. Somasundaran, *Phys. Chem. Chem. Phys.*, **2010**, 12, 14045-14056.
- 39 D. K. Padhi and K. M. Parida, *J. Mater. Chem. A*, **2014**, 2, 10300-10312.
- 40 X. Zhang, W. Shi, J. Zhu, W. Zhao, J. Ma, S. Mhaisalkar, T. L. Maria, Y. Yang, H. Zhang, H. H. Hng and Q. Yan, *Nano Res.*, **2010**, 3, 643-652.
- 41 J. Chen, L. Xu, W. Li and X. Gou, *Adv. Mater.*, **2005**, 17, 582-586.
- 42 R. Kanno, T. Shirane, Y. Kawamoto, Y. Takeda, M. Takano, M. Ohashi and Y. Yamaguchi, *J. Electrochem. Soc.*, **1996**, 143, 2435-2442.
- 43 K. F. Chen and D. Xue, *Sci China Tech Sci*, **2015**, doi: 10.1007/s11431-015-5915-z.
- 44 K. F. Chen and D. Xue, *Journal of Materiomics*, **2015**, 1, 170-187.
- 45 K. F. Chen, S. Song and D. Xue, *RSC Adv.*, **2014**, 4, 23338-23343.

Graphical Abstract



Unusual nano flowery shaped Li based iron oxides(LiFeO₂) and their pseudo capacitive behaviour